

Polar Sampling in k-Space: Reconstruction Effects

M. Louis Lauzon, Brian K. Rutt

Magnetic resonance images are most commonly computed by taking the inverse Fourier transform of the k-space data. This transformation can potentially create artifacts in the image, depending on the reconstruction algorithm used. For equally spaced radial and azimuthal k-space polar sampling, both gridding and convolution backprojection are applicable. However, these algorithms potentially can yield different resolution, signal-to-noise ratio, and aliasing characteristics in the reconstructed image. Here, these effects are analyzed and their tradeoffs are discussed. It is shown that, provided the modulation transfer function and the signal-to-noise ratio are considered together, these algorithms perform similarly. In contrast, their aliasing behavior is different, since their respective point spread functions (PSF) differ. In gridding, the PSF is composed of the mainlobe and ringlobes that lead to aliasing. Conversely, there are no ringlobes in the convolution backprojection PSF, thus radial aliasing effects are minimized. Also, a hybrid gridding and convolution backprojection reconstruction is presented for radially nonequidistant k-space polar sampling.

Key words: polar sampling; gridding; convolution backprojection; reconstruction; modulation transfer function; signal-to-noise-ratio; aliasing.

INTRODUCTION

Magnetic resonance images are most commonly calculated from the inverse Fourier transform (IFT) of the acquired k-space data. Since the data are discrete, as opposed to continuous, the sampling process may introduce image artifacts. Also, these artifacts may depend on the reconstruction algorithm used. For uniform k-space polar sampling, i.e., equally spaced radial and azimuthal samples, the images may be reconstructed by using either the gridding algorithm (1–4) or the convolution backprojection algorithm (5–7).

Gridding is a general reconstruction algorithm that can be used for any noncartesian sampling scheme. Convolution backprojection, however, applies mostly to data sampled on a purely polar grid, although other polar-type acquisitions can be reconstructed with this algorithm

(e.g., CT fan-beam, and CT cone-beam acquisitions). These two algorithms offer different tradeoffs regarding image resolution, signal-to-noise ratio (SNR), and aliasing in the reconstructed image. Since these effects may adversely influence the appearance and subsequent analysis of the image content, the choice of reconstruction algorithm is important. The purpose of this study is to compare the resolution, SNR, and aliasing characteristics of these two reconstruction algorithms.

In the Theory section, we analyze the modulation transfer function (MTF), the SNR, and the aliasing effects of equally spaced radial and azimuthal polar magnetic resonance (MR) data reconstructed by using both gridding and convolution backprojection. In the Tradeoffs section, we discuss the tradeoffs of gridding versus convolution backprojection. We also discuss practical SNR improvements with either reconstruction method. Experimental verification of the theory is presented in the Results section. In the Nonequidistant k_r Sampling section, we discuss the potential benefits of a hybrid gridding and convolution backprojection reconstruction applicable to radially nonequidistant but azimuthally equidistant polar k-data.

THEORY

Gridding

Gridding (GRD) is a general purpose Fourier reconstruction algorithm. It is flexible in that any noncartesian samples are interpolated onto a cartesian rectilinear grid and then transformed using the rapid and efficient fast Fourier transform (FFT) (8), which operates on discrete data.

Algorithm Description

Let us assume that the MR magnetization in n -dimensional k-space is given by $M(\mathbf{k})$. In the acquisition process, we sample the magnetization, either rectilinearly or not, via the function $S(\mathbf{k})$, which consists of unit area δ -functions at the appropriate locations in k-space. The acquired sampled magnetization is given by

$$M_s(\mathbf{k}) = M(\mathbf{k})S(\mathbf{k}) \quad [1]$$

Since the k-space sampling density may be nonuniform for some general acquisition k-trajectory, each sample at location \mathbf{k} is weighted by its areal extent, say $W(\mathbf{k})$. The sampled and weighted magnetization is then interpolated (i.e., regridded) onto a cartesian k-space grid via convolution and resampling, namely

$$M_{\text{swcs}}(\mathbf{k}) = \{[M_s(\mathbf{k})W(\mathbf{k})] \star C(\mathbf{k})\} \times \frac{1}{\Delta\mathbf{k}} \text{III}\left(\frac{\mathbf{k}}{\Delta\mathbf{k}}\right) \quad [2]$$

where $C(\mathbf{k})$ is the interpolating function,

$$(1/\Delta\mathbf{k})\text{III}((\mathbf{k}/\Delta\mathbf{k}))$$

MRM 40:769–782 (1998)

From the Department of Medical Biophysics (M.L.L., B.K.R.), University of Western Ontario, London, Ontario, Canada; The Tom Lawson Family Imaging Research Labs (M.L.L., B.K.R.), John P. Roberts Research Institute, London, Ontario, Canada; and the Department of Diagnostic Radiology and Nuclear Medicine (B.K.R.), London Health Sciences Centre, London, Ontario, Canada.

Address correspondence to: Brian K. Rutt, PhD, FCCPM, The Tom Lawson Family Imaging Research Labs, John P. Roberts Research Institute, 100 Perth Dr., PO Box 5015, London, Ontario, Canada N6A 5K8.

Received January 10, 1997; revised November 7, 1997; accepted April 29, 1998.

This work was supported by the Medical Research Council of Canada.

0740-3194/98 \$3.00

Copyright © 1998 by Lippincott Williams & Wilkins

All rights of reproduction in any form reserved.

is the n -dimensional cartesian sampling function of spacing $\Delta \mathbf{k}$ in the \mathbf{k} directions, \star denotes convolution, and \times denotes multiplication.

The inverse FFT, denoted FFT^{-1} , is then used to reconstruct the regridded MR image, say $I_{\text{grd}}(\mathbf{r})$. However, by the Fourier convolution theorem (ref. 9, p. 108), convolution with $C(\mathbf{k})$ in Fourier space implies apodization by $c(\mathbf{r})$ in image space, where $c(\mathbf{r})$ is the IFT of $C(\mathbf{k})$. To undo this effect, one must divide the inverse FFT of $M_{\text{swcs}}(\mathbf{k})$ by $c(\mathbf{r})$, so that

$$I_{\text{grd}}(\mathbf{r}) = \frac{1}{c(\mathbf{r})} \text{FFT}^{-1}\{M_{\text{swcs}}(\mathbf{k})\} \quad [3]$$

Modulation Transfer Function

It is customary to describe an imaging system by its frequency response, also known as its transfer function (10). The transfer function provides a useful measure of the system's behavior and allows for a direct comparison between systems.

If the input to a linear system is $f(\mathbf{r})$, linear systems theory predicts the output to be $f(\mathbf{r}) \star p(\mathbf{r})$, where $p(\mathbf{r})$ is the point spread function (PSF) of the system, i.e., the response to an impulse function. In frequency space this becomes $F(\mathbf{k}) P(\mathbf{k})$, where $F(\mathbf{k})$ and $P(\mathbf{k})$ are the Fourier transforms of $f(\mathbf{r})$ and $p(\mathbf{r})$, respectively. The transfer function $P(\mathbf{k})$ describes how each frequency is modulated according to $|P(\mathbf{k})|e^{i\phi_p(\mathbf{k})}$. More specifically, $|P(\mathbf{k})|$ and $\phi_p(\mathbf{k})$ are the modulation (MTF) and phase transfer functions, respectively. Note that if the PSF is an even function, then the transfer function is purely real, whereby the phase transfer function can only assume values of 0 or π . This is the case with GRD (and convolution back-projection), and so an MTF analysis suffices.

For a point object, $M(\mathbf{k})$ is unity over all of \mathbf{k} -space. Consequently, $M_s(\mathbf{k})$ is unity at all discrete locations in Eq. [2], and $M_{\text{swcs}}(\mathbf{k})$ is also unity at each regridded cartesian \mathbf{k} location, even though the sampling density is nonuniform. In other words, after regridding (interpolation and resampling) the energy per unit area is constant; this is a consequence of the $W(\mathbf{k})$ weighting directly compensating for the varying sample density. In the particular case of purely polar sampling, the ramp weighting leads to the GRD algorithm's MTF being unity throughout the acquisition region, i.e., within the radial frequency range $[0, k_r^{\text{max}}]$, where $k_r^{\text{max}} = \frac{1}{2}N_r\Delta k_r$.

The theoretical MTF expectations for GRD reconstruction of polar \mathbf{k} -data were verified via numerical simulations. Analytical \mathbf{k} -space values of noise-free image domain sinusoidal bar phantoms were calculated. All synthetic phantoms were derived from assumed unit amplitude (x -directional) sinusoids given by $1 + \sin((2\pi x N_c / \text{FOV}))$, where x is within the range $\pm \text{FOV}/2$, and N_c is the number of sinusoid cycles per FOV. To avoid leakage artifacts, N_c was chosen to be an integral number of cycles. The reconstructed bar phantom amplitude for $N_c = 1$ was then normalized to unity, and all other reconstructed N_c phantoms were scaled accordingly. Thus, the relative amplitudes of the reconstructed sinusoidal bar phantoms yielded the MTF values directly. Moreover, to avoid secondary sampling effects

(i.e., a beat frequency), N_c was chosen to be a factor of N_r , the number of discrete image points per FOV. For example, with $N_r = 192$, the available N_c values were $\{1, 2, 3, 4, 6, 8, 12, 16, 24, 48\}$. The measured synthetic sinusoid amplitudes (MTF values) were 1.00 ± 0.01 .

Signal-to-Noise Ratio

In any real physical system, the true signal is accompanied by noise that corrupts the image. In MRI, it is the measured \mathbf{k} -data that include a noise term, say $\eta(\mathbf{k})$. We assume that $\eta(\mathbf{k})$, the input noise function, is a zero-mean complex uncorrelated Gaussian additive stochastic quantity with SD σ . Note that such noise is strictly true only in the case of an ideal low pass (rectangular) analog-to-digital acquisition filter. Under this assumption, the duration time of acquisition (T_{acq}) scales the expectation value according to

$$E[\eta(\mathbf{k}_1)\eta^*(\mathbf{k}_2)] = \frac{\sigma^2}{T_{\text{acq}}} \delta(\mathbf{k}_1 - \mathbf{k}_2) \quad [4]$$

where $\delta(\star)$ is the impulse function, and the \star superscript denotes the complex conjugate. Under these conditions, and the underlying assumption that the samples are acquired with constant dwell time, Pipe and Duerk (11) have shown that the variance (per unit \mathbf{k} -space coverage) of the reconstructed noise is given by

$$\text{var} = \frac{\sigma^2}{T_{\text{acq}} \text{Area}_k^2} \int_k |W(\mathbf{k})|^2 d\mathbf{k} \quad [5]$$

where $W(\mathbf{k})$ is the GRD-weighting function, and Area_k is the entire area of \mathbf{k} -space covered during data acquisition. For 2D purely polar sampling, the product of the sampling and weighting functions, i.e., $S(\mathbf{k})W(\mathbf{k})$, is given by

$$\sum_{n=0}^{N_a-1} \sum_{m=-N_r/2}^{N_r/2-1} \delta(k_x - m\Delta k_r \cos n\Delta k_\theta), \quad [6]$$

$$k_y - m\Delta k_r \sin n\Delta k_\theta |m|(\Delta k_r)^2 \Delta k_\theta$$

As expected, the weighting for the $[N_r \times N_a]$ polar samples depends on the radial location $|m|\Delta k_r$, which is the ramp filter. Note that we have N_a azimuthal samples within $0 - \pi$ to be consistent with the convolution back-projection convention, i.e., $\Delta k_\theta = (\pi/N_a)$.

Although the ramp filter may not be the "optimal" weighting function (in terms of noise reduction and smoothing), it is the most intuitive one and can be directly compared with convolution backprojection using the Ram-Lak (ramp) filter. An apodized ramp filter of the form $\mathcal{A}(k_r)|m|\Delta k_r$ may prove more beneficial in practice, although this would alter the GRD MTF. Here, however, we deal strictly with the unapodized ramp filter, namely $\mathcal{A}(k_r) = 1$, from which the GRD variance per unit of \mathbf{k} -space coverage is given by

$$\text{var}_{\text{grd}} = \frac{\sigma^2 \sum_n \sum_m [\mathcal{A}(k_r)|m|(\Delta k_r)^2 \Delta k_\theta]^2}{T_{\text{acq}} [\pi(N_r \Delta k_r / 2)^2]^2} = \frac{4\sigma^2}{3T_{\text{acq}} N_r N_a} \quad [7]$$

Since the normalized SNR is given by the reciprocal of the square root of the variance, then

$$\text{SNR}_{\text{grd}} \approx \frac{\sqrt{3 T_{\text{acq}} N_r N_a}}{2\sigma} \quad [8]$$

Note that this effectively represents the SNR *per unit voxel volume*. According to Edelstein *et al.* (12) and Macovski (13), the SNR scales as the voxel volume Δv , given by $\Delta x \Delta y \Delta z$ with Δz the slice thickness. Thus,

$$\text{SNR}_{\text{grd}} \approx \frac{\Delta v \sqrt{3 T_{\text{acq}} N_r N_a}}{2\sigma} \quad [9]$$

Experimental verification of the $\sqrt{T_{\text{acq}}}$ and Δv dependence are given in the Results section.

Aliasing

Since the magnetization is sampled via $S(\mathbf{k})$, the k -data are discrete as opposed to continuous, and the reconstructed image is the true image convolved with the point spread function, which is the IFT of $S(\mathbf{k})W(\mathbf{k})$. The process of discretization, then, can potentially lead to aliasing artifacts.

For finite extent polar sampling, the principal polar PSF can be determined by considering $\frac{1}{2}N_r$ concentric rings spaced by Δk_r . Using the formalism of Bracewell and Thompson (14), Lauzon and Rutt (15) have shown that the polar PSF is given by the spin integration of $\psi(r)$, where $\psi(r)$ is the 1D IFT of the discrete (as opposed to continuous) ramp filter, which is the weighting function of Eq. [6]. Thus,

$$\begin{aligned} \psi(r) &= \mathcal{F}^{-1}\{W(k_r)\} \\ &= \mathcal{F}^{-1}\left\{\sum_{m=-N_r/2}^{N_r/2-1} |m\Delta k_r| \delta(k_r - m\Delta k_r)\right\} \\ &= \frac{(N_r\Delta k_r)^2}{4} \left[2 \text{sinc}(rN_r\Delta k_r) \right. \\ &\quad \left. - \text{sinc}^2\left(\frac{1}{2}rN_r\Delta k_r\right) \right] \star \Delta k_r \text{III}(r\Delta k_r) \\ &= \frac{(N_r\Delta k_r)^2}{4} \sum_{j=-\infty}^{\infty} \left\{ 2 \text{sinc}\left(\left[r - \frac{j}{\Delta k_r}\right]N_r\Delta k_r\right) \right. \\ &\quad \left. - \text{sinc}^2\left(\frac{1}{2}\left[r - \frac{j}{\Delta k_r}\right]N_r\Delta k_r\right) \right\} \end{aligned} \quad [10]$$

where \mathcal{F}^{-1} denotes the IFT operator, and $\text{sinc}(\xi) = (\sin(\pi\xi)/\pi\xi)$. The spin integration of $\psi(r)$, denoted $\mathcal{Q}\{\psi(r)\}$, is identical with backprojecting $\psi(r)$ continuously (as opposed to discretely) at all angles from 0 to π . In doing so, we obtain the principal polar PSF, namely

$$\text{PSF}_{\text{grd}} = s_0(r) + \sum_{j=1}^{\infty} s_j(r) \begin{cases} s_0(r) = \mathcal{Q}\{\psi_0(r)\} \\ s_j(r) = \mathcal{Q}\{\psi_+(r) + \psi_-(r)\} \end{cases} \quad [11]$$

where $s_0(r)$ and $s_j(r)$ are the main lobe and ringlobes, respectively, \mathcal{Q} is the spin integration operator, and $\psi_j(r)$ is one term of Eq. [10] at that particular j value.

On evaluation, $s_0(r)$ behaves as $(J_1(\pi r N_r \Delta k_r) / \pi r N_r \Delta k_r)$ (the jinc function; see ref. 9, p. 249), which is the circular analog of the sinc function. It describes the blurring effect of having sampled over a *finite* extent. The ringlobes $s_j(r)$ are oscillatory and asymmetrical in the radial direction, with their peak amplitude occurring near $(j/\Delta k_r)$. The ringlobe peak amplitudes decay with the ringlobe order as $(1/\sqrt{j})$. A more in-depth analysis of the characteristics of the polar PSF main lobe and ringlobes is presented in ref. 15.

The resultant image, then, is a summation of the true object convolved with (1) the main lobe $s_0(r)$, which replicates the object at $r = 0$ and blurs it due to finite sampling; and (2) with the ringlobes $s_j(r)$, which smear the object azimuthally and radially at multiple radii $(j/\Delta k_r)$. Furthermore, if the k -space values are not sufficiently sampled in the azimuthal direction, then streak artifacts (azimuthal aliasing) will also result. To avoid this type of aliasing, one requires $N_a \geq \frac{1}{2}\pi N_r$.

Although GRD is an optimized interpolation and reconstruction technique (with the appropriate choice of convolution function), it does not correct for the original sampling effects (4). In other words, the 2D polar PSF in Eq. [11] affects the aliasing at a level that is not remedied by using GRD. In practice, the regridded k -data are sub-sampled (say by the "oversampling" factor "ovr") onto a finer cartesian k -grid. Upon IFFT, the resultant image FOV is larger by the same factor "ovr." The true object is then cropped from the central $(1/\text{ovr})^{\text{th}}$ region. This sub-sampling process minimizes any aliasing from the reinterpolation and subsequent IFFT, but it does *not* correct for the inherent aliasing effects incurred during acquisition.

Consequently, the overall signal amplitude distribution of the object may be compromised, as shown in Fig. 1: as the object becomes larger relative to the FOV, the aliasing leads to a greater deviation of the signal amplitude profile distribution. The GRD images were regridded using the Kaiser-Bessel window function (an approximation to the Prolate Spheroidal Wave Function of zero order) given by $I_0(\beta\sqrt{1 - (2k/L)})$, with parameters $L = 4$, $\beta = 12$, and a subsampling factor of $\text{ovr} = 2$. These parameters apply to both the k_x and k_y directions, and for all GRD reconstructions within this study. These parameters were chosen in such a manner to minimize uniformity deviations (in the least-squares sense) of an expected uniform synthetic disk phantom occupying 50% of the FOV. We fixed the oversampling parameter to $\text{ovr} = 2$, and varied L and β within 3–6 and 6–20, respectively. Within this range of parameters, the measured uniformity deviations were similar, which suggests that the gridding reconstruction is not overly sensitive to the choice of the L and β parameters.

The sampling effects of purely polar sampling can be minimized if one sinc interpolates in the radial k_r direction before regridding. This is most easily accomplished by taking the 1D IFT of the radial k_r lines, zero-padding to twice their length, and Fourier transforming back to k -space. Gridding can then be used by applying the dis-

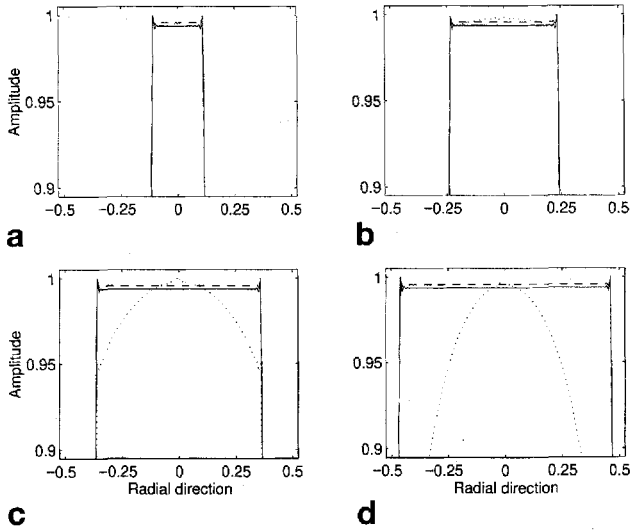


FIG. 1. Synthetic, noise-free, uniform disk profiles of reference cartesian k -data reconstructed with the FFT (solid line), and of polar k -data reconstructed using GRD (dotted line) or CBP (dashed line). The GRD reconstruction kernel parameters can be found in the text. The radial axes are in units of the FOV. The profiles are for disk diameters of (a) 25% of the FOV, (b) 50% of the FOV, (c) 75% of the FOV, and (d) 95% of the FOV. Note the increasing nonuniform profile signal amplitude for GRD as the object size increases, an aliasing effect arising from the ringlobes $s_j(r)$.

crete ramp weighting (whose spacing is now $\frac{1}{2}\Delta k_r$). In this case, the polar PSF is given by $s_0(r) + \sum_{j=1}^{\infty} s_{2j}(r)$. Since the first ringlobe $s_1(r)$ and all odd-order ringlobes have been eliminated, the reconstructed image has reduced aliasing.

For example, an object occupying 95% of the FOV may deviate from its true signal amplitude distribution by as much as 20% if GRD is performed on the original k -data, as shown in Fig. 1d. However, by sinc interpolating in the k_r direction by a factor of 2 *before* gridding, the signal amplitude deviations are within 1% owing to the reduced aliasing. Similarly, by sinc interpolating in the k_r direction by a factor of 4 *before* gridding, the deviation is within 0.1% for the same object, since the polar PSF now consists of the main lobe and every fourth ringlobe, i.e., $s_0(r) + \sum_{j=1}^{\infty} s_{4j}(r)$. For general noncartesian sampling schemes, however, sinc interpolation in the k_r direction may neither be practical nor possible.

Convolution Backprojection

The convolution backprojection (CBP) algorithm has been used extensively in CT. Although CT acquires data in the image domain, i.e., real projections through the object, by using the central slice theorem (16) one can show that this is equivalent to polar sampling in k -space. Furthermore, CBP may be applied to (noisy) complex projections, since one can reconstruct the real and imaginary components independently. Therefore, CBP has potential applications to MR reconstruction.

Algorithm Description

The reconstructed MR image is given by the inverse Fourier transform of the sampled magnetization, $M_s(k)$. If

one expresses the Fourier variables in polar notation ($k_x = k_r \cos k_\theta$, $k_y = k_r \sin k_\theta$), the polar sampled magnetization can be written as

$$M_s(k_r, k_\theta) = \sum_{n=0}^{N_a-1} \sum_{m=-N_r/2}^{N_r/2-1} M(m\Delta k_r, n\Delta k_\theta) \delta(k_r - m\Delta k_r, k_\theta - n\Delta k_\theta) \Delta k_r \Delta k_\theta \quad [12]$$

$$\equiv \Delta k_r \Delta k_\theta \sum_{n=0}^{N_a-1} \sum_{m=-N_r/2}^{N_r/2-1} M_n(m\Delta k_r) \delta(k_r - m\Delta k_r, k_\theta - n\Delta k_\theta)$$

where $M_n(m\Delta k_r)$ is the magnetization sampled in the k_r direction at angle $n\Delta k_\theta$. With the use of Eq. [A5] from Appendix A, the reconstructed CBP image is given by

$$I_{cbp}(x, y) = \Delta k_r \Delta k_\theta \sum_{n=0}^{N_a-1} \mathcal{B}\{\text{FFT}^{-1}[M_n(m\Delta k_r)] \star C_{cbp}(r)\} \quad [13]$$

where \mathcal{B} is the backprojection operator, $C_{cbp}(r)$ is the discrete convolution function sampled at spacing $\Delta r = (1/N_r\Delta k_r)$, and the term being backprojected is the discrete convolved MR "projection" at angle $n\Delta k_\theta$. The image is summed over all N_a convolved projections being backprojected at the desired cartesian (x, y) locations.

The convolution function is effectively given by the sampled IFT of the finite *continuous* (as opposed to discrete) ramp filter $|k_r|$. To reduce high frequency aliasing/leakage, this filter is often apodized by $\mathcal{A}(k_r)$ so that in general C_{cbp} is given by

$$C_{cbp}(r) = \mathcal{F}^{-1}\left\{\mathcal{A}(k_r) \left|k_r\right| \Pi\left(\frac{k_r}{N_r\Delta k_r}\right)\right\} \times \frac{1}{\Delta r} \Pi\left(\frac{r}{\Delta r}\right) \quad [14]$$

where $\Pi(\xi) = 1$ for $|\xi| \leq \frac{1}{2}$ and 0 otherwise.

For a direct comparison of the CBP and GRD algorithms, we limit ourselves to the ramp filter (known as the Ram-Lak filter in the CT community) whereby $\mathcal{A}(k_r) = 1$, in analogy to the GRD case. A brief overview of the tradeoffs of apodized ramp filters is given in the Tradeoffs section. The CBP reconstruction algorithm may be applied to any type of purely polar k -data, be it Hermitian, anti-Hermitian, or non-Hermitian (see Appendix A).

Modulation Transfer Function

The convolution backprojection MTF is dependent on three factors: (1) the convolution function $C_{cbp}(r)$, which weights the projections (in the image domain); (2) the interpolation function used in the backprojection stage; and (3) the resampling onto the image grid.

The interpolation arises because each desired image (x, y) location corresponds to a given projected location onto the 1D convolved MR projection vector at angle $n\Delta k_\theta$. These projected locations may or may not coincide with an actual MR projection sample located at $(p/N_r\Delta k_r)$, with $p = \{-(N_r/2), \dots, (N_r/2) - 1\}$. Thus, some interpolation is required so that the appropriate MR projection value is backprojected to each desired image pixel location.

Various filter (apodized ramp) functions and their convolution counterparts appear in Jain (17, Ch. 10), although we will analyze only the case for the Ram-Lak (unapodized ramp) filter (18). Of course, the analysis below follows readily for any filter function. In the case of the Ram-Lak filter, $C_{cbp}(r)$ of Eq. [14] is easily calculated and the coefficients are given in Appendix B.

After discrete convolution of the projections with $C_{cbp}(r)$, one must backproject these onto the image grid: this requires both interpolation and resampling. One of the more computationally efficient and commonly used interpolation techniques is linear interpolation, which is assumed here. It can be expressed as a convolution (in the image domain) with a triangle function of width $2\Delta r = (2/N_r \Delta k_r)$. In k -space, this corresponds to a modulation of $\text{sinc}^2((k_r/N_r \Delta k_r))$.

The convolved interpolated projection is then backprojected and resampled onto the desired image locations. This resampling leads to some form of wraparound in the 2D k -space, the details of which can be found in Appendix B.

The algorithm's MTF can be calculated for large N_a ($N_a \geq 16N_r$) if $M_n(m\Delta k_r) = 1$ for all m . In this case, the MR projections ($\text{FFT}^{-1}\{M_n\}$) are given by a single impulse function at $r = 0$. Reconstruction of these data yields the algorithm's PSF, since we expect to reconstruct a point at the image center. Finally, the Fourier transform magnitude of the PSF gives the MTF.

The Ram-Lak MTF contour is given in Fig. 2. For comparison, that of the Shepp-Logan filter (an apodized ramp) is also shown. Note that the MTFs are *not* circularly symmetric, nor are they confined to a circle of diameter $N_r \Delta k_r$, even though the acquired data are within that circle. These effects arise because of the interpolation and resampling during backprojection, as discussed in Appendix B. However, at low frequencies these

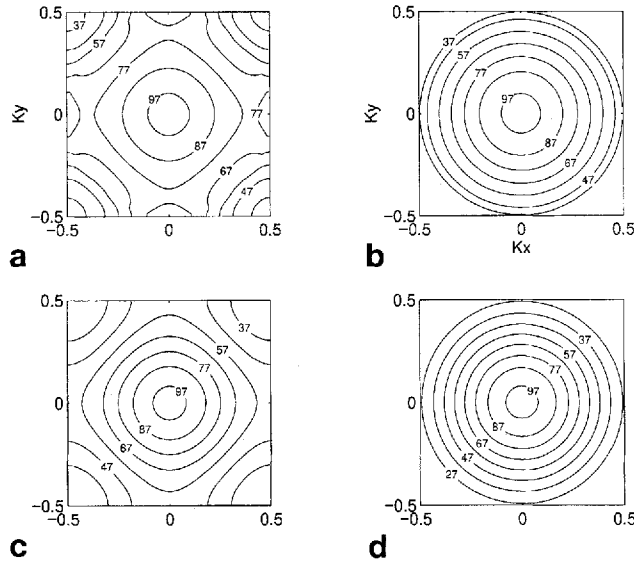


FIG. 2. Contour percentages of CBP MTFs. The axes are in units of $N_r \Delta k_r$. (a) True MTF using the Ram-Lak filter; (b) truncated $\text{sinc}^2((k_r/N_r \Delta k_r))$; (c) true MTF using the Shepp-Logan filter; (d) truncated $\text{sinc}^3((k_r/N_r \Delta k_r))$. Note that the true MTFs are fourfold symmetric, whereas the truncated sinc^2 and sinc^3 approximations are circularly symmetric.

MTFs can be approximated by the circularly symmetric functions $\text{sinc}^2((k_r/N_r \Delta k_r))$ and $\text{sinc}^3((k_r/N_r \Delta k_r))$, respectively. These approximations are also depicted in Fig. 2.

The MTF values were verified with simulations. The synthetic phantom k -values were calculated in the same manner as that for GRD (see Modulation Transfer Function section), and the images were reconstructed by using CBP. The theoretical MTF values on axis for $N_r = 192$, and N_c assuming values of {1, 2, 3, 4, 6, 8, 12, 16, 24, 48} are {1.000, 0.999, 0.998, 0.998, 0.996, 0.994, 0.988, 0.979, 0.955, 0.848}, respectively. The measured synthetic sinusoid amplitudes (the MTF values) were within $\pm 2\%$ of these theoretical values.

Signal-to-Noise Ratio

As in GRD, we assume that the k -space noise term is a zero-mean uncorrelated complex additive Gaussian stochastic variable with SD σ . The variance analysis of Pipe and Duerk (11) for GRD reconstruction, as given in Eq. [5], is equally valid for the CBP reconstruction. Thus, the variance per unit k -space coverage is still given by

$$\text{var} = \frac{\sigma^2}{T_{\text{acq}} \text{Area}_k^2} \int_k |W(\mathbf{k})|^2 d\mathbf{k} \quad [15]$$

where $W(\mathbf{k})$ is the *effective* weighting function in k -space, namely the CBP convolution function before IFT times the appropriate MTF. In the previous section, we showed that the convolution function, backprojection, and resampling operations lead to a nonuniform MTF in k -space. Consequently, the variance-weighting function must incorporate these effects. This is done by multiplying the (perhaps apodized) ramp function with the calculated CBP MTF. Consequently, the CBP variance per unit k -space coverage is given by

$$\begin{aligned} \text{var}_{\text{cbp}} &= \frac{\sigma^2 \sum_{n=0}^{N_a-1} \sum_{m=-N_r/2}^{N_r/2-1} [\mathcal{A}(m\Delta k_r) |m\Delta k_r| \cdot \text{MTF}(m\Delta k_r, n\Delta k_\theta) \Delta k_r \Delta k_\theta]^2}{T_{\text{acq}} [\pi(N_r \Delta k_r / 2)^2]^2} \quad [16] \end{aligned}$$

More particularly, var_{cbp} using the Ram-Lak (rala) filter is calculated using $\mathcal{A}(m\Delta k_r) = 1$ and the Ram-Lak MTF (shown in Fig. 2), so that

$$\begin{aligned} \text{var}_{\text{rala}} &= \frac{\sigma^2 \sum_{n=0}^{N_a-1} \sum_{m=-N_r/2}^{N_r/2-1} [|m\Delta k_r| \text{MTF}_{\text{rala}}(m\Delta k_r, n\Delta k_\theta) \Delta k_r \Delta k_\theta]^2}{T_{\text{acq}} [\pi(N_r \Delta k_r / 2)^2]^2} \\ &\approx 0.711 \frac{\sigma^2}{T_{\text{acq}} N_r N_a} \quad [17] \end{aligned}$$

Since the CBP MTF is difficult to ascertain analytically, we resorted to a numerical evaluation of the variance per unit k -space coverage. Therefore, the 0.711 factor comes about from a numerical integration of the square of the

finite, circular, ramp filter multiplied by the Ram-Lak MTF divided by the circular k -space area squared.

Using Eqs. [9] and [17], and $\text{SNR} = (\Delta v / \sqrt{\text{var}})$, the CBP_{rala} SNR relative to GRD of polar data using the ramp filter is easily compared, as given in Table 1. The Shepp-Logan results are also included for additional comparison. The CBP algorithm implemented with the Ram-Lak filter yields an increased SNR relative to GRD of

polar k -data using the ramp filter. However, with GRD, the MTF is flat whereas with CBP the MTF decreases at higher frequencies, resulting in a loss of resolution. This point will be expounded on in the Tradeoffs section.

Aliasing

The aliasing using the CBP algorithm of Eq. [13] is markedly different than that of GRD. Because the radial k_r -lines are discretized rectilinearly with spacing Δk_r , the Nyquist criterion applies in the radial direction: if the object is spatially limited to within a diameter of $(1/\Delta k_r)$, then the inverse FFT of each radial k_r -line is a nonaliased projection through the object. Thus, unlike GRD, in CBP the original sampling effects in the k_r direction are treated in 1D as opposed to 2D.

The azimuthal sampling criterion, however, remains the same between the two algorithms: if the k -space values are azimuthally undersampled, the reconstructed image will contain streak artifacts. If, however, $N_a \geq \frac{1}{2}\pi N_r$, then the image will not suffer from this streaking artifact.

Nevertheless, the effective PSF of CBP is similar to that of GRD, except that the PSF is composed of the main lobe *only* and *no* ringlobes. If there are an infinite number of projections, then the CBP PSF is calculated from the spin integration of $C_{\text{cbp}}(r)$ found in Eq. [14]. However, one must note that $C_{\text{cbp}}(r)$ is the IFT of the *continuous* (perhaps apodized) ramp filter followed by discretization in the image domain; in contrast, the GRD weighting function is discretized directly in k -space, from which the GRD PSF is the spin integration of the IFT of the discretized $W(\mathbf{k})$. This difference leads to the ringlobes in GRD, but not in CBP.

For example, $C_{\text{cbp}}(r)$ using the Ram-Lak filter is, from Appendix B,

$$C_{\text{cbp}}(r) = \frac{(N_r \Delta k_r)^2}{4} \quad [18]$$

$$\cdot \left[2 \text{sinc}(r N_r \Delta k_r) - \text{sinc}^2\left(r \frac{N_r}{2} \Delta k_r\right) \right] \times \frac{1}{\Delta r} \text{III}\left(\frac{r}{\Delta r}\right)$$

with $\Delta r = (1/N_r \Delta k_r)$ as before. Neglecting the sampling process, i.e., the $\text{III}(r/\Delta r)$ term, C_{cbp} above is identical with $\psi(r)$ of Eq. [10] for $j = 0$. On spin integration, the CBP PSF is given by $\mathcal{Q}\{\psi_0(r)\} = s_0(r)$. Thus, as stated previously, the PSF consists of the main lobe only and no

Table 1

Theoretically expected absolute and relative variance (var) and SNR values for $[N_r \times N_a]$ polar samples reconstructed using either GRD with the ramp filter, CBP with the Ram-Lak (rala) filter, or CBP with the Shepp-Logan (shlo) filter^a

	Polar sampling		
	GRD reconstruction	CBP _{rala} reconstruction	CBP _{shlo} reconstruction
var	$(4/3)(\sigma^2/T_{\text{acq}}N_rN_a)$	$0.711 (\sigma^2/T_{\text{acq}}N_rN_a)$	$0.448 (\sigma^2/T_{\text{acq}}N_rN_a)$
(var/var _{grd})	1	0.533	0.336
SNR	$(\sqrt{3}/2)(\Delta v/\sqrt{T_{\text{acq}}N_rN_a}/\sigma)$	$1.186 (\Delta v/\sqrt{T_{\text{acq}}N_rN_a}/\sigma)$	$1.494 (\Delta v/\sqrt{T_{\text{acq}}N_rN_a}/\sigma)$
(SNR/SNR _{grd})	1	1.370	1.725

^a Under these conditions, the effective resolution will be maximum for GRD (since its MTF is uniform), whereas that of CBP is reduced (since the MTFs roll off at higher frequencies, as depicted in Figs. 2a and 2c for the rala and shlo filters, respectively).

ringlobes. In effect, the ringlobes in GRD emanate from the sampling (in k -space) of the weighting function *before* the IFT and subsequent spin integration. Conversely, CBP eliminates the ringlobes by sampling (in the image domain) the IFT of the weighting function *after* the IFT.

In reality, the discretization of $C_{\text{cbp}}(r)$ means that the true CBP PSF is different than $s_0(r)$, the GRD main lobe. Whereas $s_0(r)$ is calculated from the spin integration of $\psi_0(r)$, in CBP one spin integrates $C_{\text{cbp}}(r)$, which is a sampled and subsequently interpolated version of $\psi_0(r)$. The functions ψ_0 and C_{cbp} are depicted on the left sides of Fig. 5a and 5e, respectively.

The CBP sampling criterion is simply stated: provided that (1) the k_r spacing Δk_r is such that the object is contained within a circle of diameter $(1/\Delta k_r)$, and (2) the number of projections N_a within the azimuthal range $0 - \pi$ is of the order $\frac{1}{2}\pi N_r$ or greater, then the aliasing resulting from the CBP reconstruction will be negligible.

TRADEOFFS

Although GRD is a general reconstruction algorithm and CBP applies mostly to polar sampling, their respective tradeoffs concerning resolution, SNR, and aliasing can be directly compared for purely polar k -space acquisitions.

The effective resolution of each algorithm is dependent on its modulation transfer function. The MTF of GRD for polar k -data using the ramp filter is unity for radial frequencies $|k_r| \leq \frac{1}{2}N_r\Delta k_r$. Conversely, the MTF of CBP using the Ram-Lak filter is not unity, nor is it circularly symmetric. Rather, it is an even fourfold symmetric function that can be approximated by $\text{sinc}^2((k_r/N_r\Delta k_r))$ at low spatial frequencies, as explained in the Convolution Backprojection-Modulation Transfer Function section.

For GRD reconstruction using the ramp weighting, the MTF is flat. Conversely, for CBP reconstruction using the Ram-Lak filter, the MTF decreases at higher spatial frequencies. Thus, the effective image resolution of CBP (rala) images is degraded with respect to that of GRD. However, this decrease in resolution is compensated by an increase in SNR, as shown in Table 1.

The weighting functions need not be limited to the ramp (Ram-Lak) functions. Many choices of apodized ramp functions are possible, both for GRD and CBP. The ramp filter guarantees the maximum resolution (for a given algorithm) in the reconstructed image. However, with the ramp filter the variance is also maximized,

which leads to a minimal SNR. For apodized ramp functions, the MTF rolls off at higher k_r -values. This leads to blurring in the image but with an increase in SNR. Thus, resolution and SNR must be considered in unison to properly compare the GRD and CBP algorithms.

In both GRD and CBP, the variance is given by the effective k -space weighting squared, namely the (possibly apodized) ramp weighting times the MTF of the reconstruction algorithm, i.e.,

$$\sum_{n=0}^{N_a-1} \sum_{m=-N_r/2}^{N_r/2-1} \cdot [\mathcal{A}(m\Delta k_r) |m\Delta k_r| \text{MTF}(m\Delta k_r, n\Delta k_\theta) \Delta k_r \Delta k_\theta]^2 \quad [19]$$

For both GRD and CBP, $\mathcal{A}(m\Delta k_r)$ is unity when using the ramp and/or Ram-Lak filters. However, their respective MTFs are different, which leads to a different variance and SNR. However, the change in SNR is directly compensated for by a change in resolution, owing to their different MTFs, as discussed earlier.

One can, in principle, restore maximum resolution by deconvolving the PSF from the reconstructed CBP image, but doing so decreases the SNR to a level similar to that of GRD images. Also, it is possible to use an apodized ramp weighting in GRD so that the image SNR is comparable to the CBP_{rala} SNR. In other words, the GRD MTF would no longer be uniform, but would roll off at higher frequencies. In this case, the GRD and CBP image resolution and SNR will be comparable.

In effect, if one reconstructs the k -data to obtain a comparable SNR between the GRD and CBP images, then the effective image resolution or blurring will also be comparable. The reverse is also true. Thus, the GRD and CBP algorithms behave similarly when one considers resolution and SNR together: GRD with the ramp filter maximizes resolution with minimal SNR, whereas CBP sacrifices resolution with a gain in SNR. Still, one can judiciously alter the weighting parameters to get comparable results between the two algorithms. However, the aliasing properties will not be significantly altered, since altering the weighting does not eliminate the ringlobes in GRD, although it may suppress them slightly.

Although SNR and resolution must be considered together, one can simultaneously maximize both provided the azimuthal spacing varies as a function of k_r such that the GRD weighting $W(k)$ is constant. Gridding of this data

Table 3

Experimental SNR measurements relative to a 32 kHz bandwidth filter (with the corresponding acquisition times in parentheses)^a

	32 kHz (6144 μ s)	16 kHz (12288 μ s)	8 kHz (24576 μ s)
GRD (11 cm)	1.000	1.380 \pm 0.074	1.952 \pm 0.123
CBP _{rala} (11 cm)	1.000	1.386 \pm 0.061	1.995 \pm 0.125
CBP _{shlo} (11 cm)	1.000	1.387 \pm 0.076	2.010 \pm 0.129
GRD (22 cm)	1.000	1.325 \pm 0.082	1.965 \pm 0.155
CBP _{rala} (22 cm)	1.000	1.333 \pm 0.120	1.930 \pm 0.215
CBP _{shlo} (22 cm)	1.000	1.294 \pm 0.105	1.893 \pm 0.197
GRD (33 cm)	1.000	1.493 \pm 0.187	1.930 \pm 0.360
CBP _{rala} (33 cm)	1.000	1.387 \pm 0.191	1.848 \pm 0.338
CBP _{shlo} (33 cm)	1.000	1.409 \pm 0.234	1.853 \pm 0.345

^a The measurements represent the mean \pm 1 SD of measured relative SNRs in 36 different ROIs within the various NiCl_2 phantoms. The theoretical expectations at 16 kHz and 8 kHz are 1.41 and 2.0, respectively.

yields maximum resolution (because of the unit MTF) and maximum SNR (19, 20), since the variance is minimized to $(\sigma^2/T_{\text{acq}}N_p)$, where N_p is the total number of sampled points. Since we require $N_a \approx \frac{1}{2}\pi N_r$ only at $k_r^{\text{max}} = \frac{1}{2}N_r\Delta k_r$, then $N_p < N_rN_a$. Thus, the reconstruction time will be shorter than for the purely polar case of $[N_r \times N_a]$ sample points. Note, however, that the aliasing characteristics will be identical in both cases because PSF_{grd} of Eq. [11] is still applicable, since there is no azimuthal aliasing.

The aliasing incurred, using CBP with the Ram-Lak filter and linear interpolation and GRD with the ramp filter, is different. For an infinite number of projections ($N_a \rightarrow \infty$), the point spread function is given by the spin integration of the appropriate function, namely Eq. [10] for GRD and Eq. [18] for CBP_{rala}. In actuality, N_a is finite and so the respective PSFs are given by a discrete and finite spin summation instead of spin integration. This leads to potential azimuthal (streaking) artifacts in the baseband unless $N_a \geq \frac{1}{2}\pi N_r$.

For GRD reconstruction, the ramp filter is discretized *before* the IFT, whereas for CBP it is discretized *after* the IFT. Because the ringlobes emanate from the discretization of the filter before the IFT, the CBP PSF is composed of the main lobe only. Thus, provided the object being reconstructed is contained within a circular FOV of diameter $(1/\Delta k_r)$ and $N_a \geq \frac{1}{2}\pi N_r$, the aliasing resulting from the CBP reconstruction will be negligible.

In comparison, the ringlobes present in the GRD PSF are due to the fact that the GRD reconstruction retains the original 2D sampling effects. One way to minimize the effects of the ringlobes is to sinc-interpolate in the radial direction before GRD reconstruction, as suggested in the Aliasing section.

It is interesting to note that if one applies the ramp (Ram-Lak) filter directly to the polar k -data before the 1D IFT (i.e., in a multiplicative fashion in analogy to what occurs in GRD), the IFT takes in the k_r direction and backprojects, then the reconstructed image aliasing is similar to that of the GRD image. This is because the IFT of the discrete ramp produces replicates that, on back-projection (the discrete analog of spin integration), lead to ringlobes. Thus, the discrete convolution in image

Table 2
Measured T_1 and T_2 relaxation times for the nickel/agarose (NiCl_2) phantoms of varying concentrations

Tube No.	NiCl_2 (mM)	Agarose (%)	T_2 (ms)	T_1 (ms)
1	5.0	4.0	24.9	249.8
2	5.0	1.0	79.4	268.2
3	5.0	0.2	178.7	270.1
4	2.0	4.0	27.3	508.4
5	2.0	1.0	95.5	573.5
6	2.0	0.2	284.0	567.1
7	0.5	4.0	27.9	1066.0
8	0.5	1.0	107.3	1230.0
9	0.5	0.2	407.7	1240.0

space is preferable to the discrete multiplication in k -space.

RESULTS

The theoretical SNR expectations were verified experimentally on a 0.5 T GE Signa scanner (General Electric Medical Systems, Milwaukee, WI). The phantom consisted of 9 NMR glass tubes (1.0 cm diameter, 15 cm length) closely packed within a $4 \times 4 \text{ cm}^2$ region. Each tube was filled with various concentrations of agarose doped with nickel chloride (NiCl_2) to generate phantoms with T_1 and T_2 values ranging from 250 to 1250 ms and 25 to 400 ms, respectively, as shown in Table 2.

A concentric circle spin echo pulse sequence was written (EPIC 5.6 pulse programming language) such that half of the circle was acquired at each excitation. The readout was in the azimuthal direction, and the radial steps were increased for subsequent excitations. The k -space values were acquired using the GE head coil and a loader shell to properly load the coil.

The MR parameters were as follows: TE of 40 ms, a TR of 2000 ms, a 5-mm slice thickness, 1 excitation (NEX) per image, a matrix size of $[384 \times 160]$ (namely 384 azimuthal points within $0 - \pi$ with 160 radial points per projection), with a scan time of 5:24 per image. The k -space values were measured for FOVs of 11, 22, and 33 cm using filter bandwidths (BW) of 32, 16, and 8 kHz, which correspond to acquisition times (T_{acq}) of 6144, 12288, and 24576 μs , respectively. All images were reconstructed onto a 256×256 image grid for both GRD and CBP.

Two images were acquired for each FOV/BW combination, e.g., img_1 and img_2 . The resultant signal and noise images were calculated from $\frac{1}{2}[\text{img}_1 + \text{img}_2]$ and $(1/\sqrt{2})[\text{img}_1 - \text{img}_2]$, respectively. The pair of images were then scaled such that the signal image was normalized to have a maximum amplitude of 100. We measured the average signal and noise within various regions of interest (ROI) of the phantoms, and determined the SNR by taking their ratio. Thirty-six ROIs were chosen within the NMR tubes, and 36 ROIs were chosen in the surrounding air medium (i.e., noise regions).

All noise images (GRD and CBP) were observed to be

Table 4
Experimental noise measurements relative to an 11-cm FOV^a

	11-cm FOV	22-cm FOV	33-cm FOV
GRD (32 kHz)	1.000	0.281 \pm 0.014	0.125 \pm 0.008
CBP _{raia} (32 kHz)	1.000	0.272 \pm 0.011	0.123 \pm 0.005
CBP _{shio} (32 kHz)	1.000	0.273 \pm 0.012	0.122 \pm 0.006
GRD (16 kHz)	1.000	0.278 \pm 0.013	0.127 \pm 0.006
CBP _{raia} (16 kHz)	1.000	0.269 \pm 0.010	0.117 \pm 0.005
CBP _{shio} (16 kHz)	1.000	0.266 \pm 0.010	0.116 \pm 0.005
GRD (8 kHz)	1.000	0.271 \pm 0.011	0.116 \pm 0.004
CBP _{raia} (8 kHz)	1.000	0.266 \pm 0.012	0.113 \pm 0.004
CBP _{shio} (8 kHz)	1.000	0.263 \pm 0.013	0.117 \pm 0.004

^a The measurements represent the mean \pm 1 SD of measured noise regions in 36 different ROIs within the air regions surrounding the NiCl_2 phantoms. The theoretical expectations at 22-cm and 33-cm FOVs are 0.25 and 0.11, respectively.

Table 5

Experimental SNR measurements of CBP_{raia} and CBP_{shio} reconstruction relative to GRD reconstruction^a

	GRD	CBP _{raia}	CBP _{shio}
11-cm FOV, 32 kHz	1.000	1.381 \pm 0.059	1.684 \pm 0.099
22-cm FOV, 32 kHz	1.000	1.367 \pm 0.047	1.719 \pm 0.088
33-cm FOV, 32 kHz	1.000	1.352 \pm 0.058	1.653 \pm 0.085
11-cm FOV, 16 kHz	1.000	1.389 \pm 0.048	1.696 \pm 0.073
11-cm FOV, 8 kHz	1.000	1.408 \pm 0.039	1.723 \pm 0.056

^a The measurements represent the mean \pm 1 SD of measured relative SNRs in 36 different ROIs within the various NiCl_2 phantoms. The theoretical expectations for CBP_{raia} and CBP_{shio} are 1.37 and 1.725, respectively.

uniform over the entire FOV. Furthermore, the signal images were observed to possess comparable signal intensities (to within $\pm 5\%$) at the various FOVs and BWs.

From Eq. [9] and Table 1, the SNRs of both GRD and CBP are expected to scale as the square root of the acquisition time. And, since $T_{\text{acq}} \propto 1/\text{BW}$, the SNRs at 16 and 8 kHz relative to that at 32 kHz are expected to increase by $\sqrt{2} \approx 1.41$ and $\sqrt{4} = 2$, respectively. The experimental results of Table 3 support the theoretical expectations.

We also verified the noise dependence with voxel volume. Since the reconstructed images consist of N_r square pixels of width Δr , the FOV along the x and y directions is given by $\text{FOV} = N_r \Delta r$. Consequently, the voxel volume is $\Delta v = \text{FOV}^2 \Delta z / N_r^2$. All images were acquired for Δz and N_r held constant, so that Δv scales as FOV^2 .

The mean noise value was measured in 36 air regions at different FOVs for various BWs for both GRD and CBP reconstruction. Since the SNR is expected to scale as FOV^2 and the maximum signal within all images was normalized to unity, then the variation of noise only is expected to scale as $1/\text{FOV}^2$. Thus, relative to an 11-cm FOV, the expected noise at 22 and 33 cm FOVs is expected to be $1/2^2 = 0.25$ and $1/3^2 \approx 0.11$, respectively. The experimental results of Table 4 support the expectations, although there seems to be a bias to slightly overestimate the noise contribution.

Finally, we verified the theoretically expected SNR increases of CBP images relative to GRD images, as given in Table 1. We expected a SNR increase of approximately 1.37 using the Ram-Lak filter, and an increase of about 1.725 using the Shepp-Logan filter. The results of Table 5 correlate well with the theoretical predictions.

Although the Gridding and Convolution Backprojection Signal-to-Noise Ratio theory sections were developed assuming ideal conditions, the results of Tables 3–5 provide experimental validation of the simplified theoretical analysis.

NONEQUIDISTANT k_r SAMPLING

The SNR, resolution, and aliasing characteristics are important design (and reconstruction algorithm) considerations for any MR acquisition. However, the scan time and the resulting flow/motion artifacts in the image are just as important. Since the gross features of the imaged object are contained near the center of k -space, whereas its edge information is located at the high spatial frequencies, it may be desirable to sample nonuniformly in the

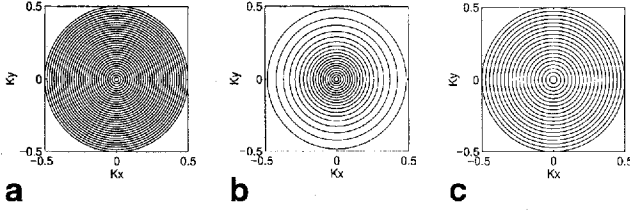


FIG. 3. k -Space sampling patterns for (a) purely polar samples with radial spacing Δk_r , (b) radially nonequidistant polar samples whose radial distribution is given in Eq. [24], and (c) purely polar samples with radial spacing $1.52\Delta k_r$. Note that all trajectories cover the same effective area in k -space. The axes are in units of $N_r\Delta k_r$.

radial and/or azimuthal directions to reduce scan time and suppress motion artifacts. Here, we restrict ourselves to nonequidistant radial polar sampling with equally spaced azimuthal samples.

To reconstruct such radially nonequidistant polar k -data, GRD can still be used because of its flexibility and generality, provided that the 2D weighting function $W(\mathbf{k})$ is known. CBP, however, expects the projection data (i.e., the 1D IFT of the k_r -lines) to be equally spaced. Consequently, one can perform a 1D GRD of the k_r -lines (which gives rectilinear MR projections) followed by CBP: this we call the hybrid GRD/CBP reconstruction.

To perform the GRD/CBP reconstruction, one first needs to determine the 1D weighting function $W(k_r)$ required in the 1D GRD of the nonequidistant k_r samples. This is easily calculated. For example, assume three consecutive k_r samples are located at $k_{r,p-1}$, $k_{r,p}$, and $k_{r,p+1}$. The weighting of the p^{th} sample, a measure of its areal extent, is given by

$$W(k_{r,p}) = \frac{1}{2} |k_{r,p} - k_{r,p-1}| + \frac{1}{2} |k_{r,p+1} - k_{r,p}| \quad [20]$$

Although GRD/CBP reconstruction is generally more time-consuming than 2D GRD, it does offer some benefits: $W(k_r)$ is easily calculated (as shown above), and the aliasing is reduced.

The aliasing reduction of GRD/CBP compared with 2D GRD is obvious when one compares their PSFs, which

are given by the spin integration of the effective weighting functions. For general nonuniform radial polar sampling, the (k_x, k_y) coordinates are transformed to $(K(k_r), k_\theta)$, where $K(k_r)$ represents some general function. For 2D GRD, the weighting is

$$W(\mathbf{k}) = \begin{vmatrix} \frac{\partial k_x}{\partial k_r} & \frac{\partial k_x}{\partial k_\theta} \\ \frac{\partial k_y}{\partial k_r} & \frac{\partial k_y}{\partial k_\theta} \end{vmatrix}_{k_r = m\Delta k_r} \Rightarrow \left| K(m\Delta k_r) \frac{dK(m\Delta k_r)}{dk_r} \right| \quad [21]$$

so that the PSF, using the Fourier convolution theorem, is given by

$$\begin{aligned} \text{PSF}_{\text{grd}} &= \mathfrak{D} \left\{ \mathcal{F}^{-1} \left[\left| K(m\Delta k_r) \frac{dK(m\Delta k_r)}{dk_r} \right| \right] \right\} \\ &= \mathfrak{D} \left\{ \mathcal{F}^{-1} \left[\left| \frac{dK(m\Delta k_r)}{dk_r} \right| \right] \star \mathcal{F}^{-1} [K(m\Delta k_r)] \right\} \end{aligned} \quad [22]$$

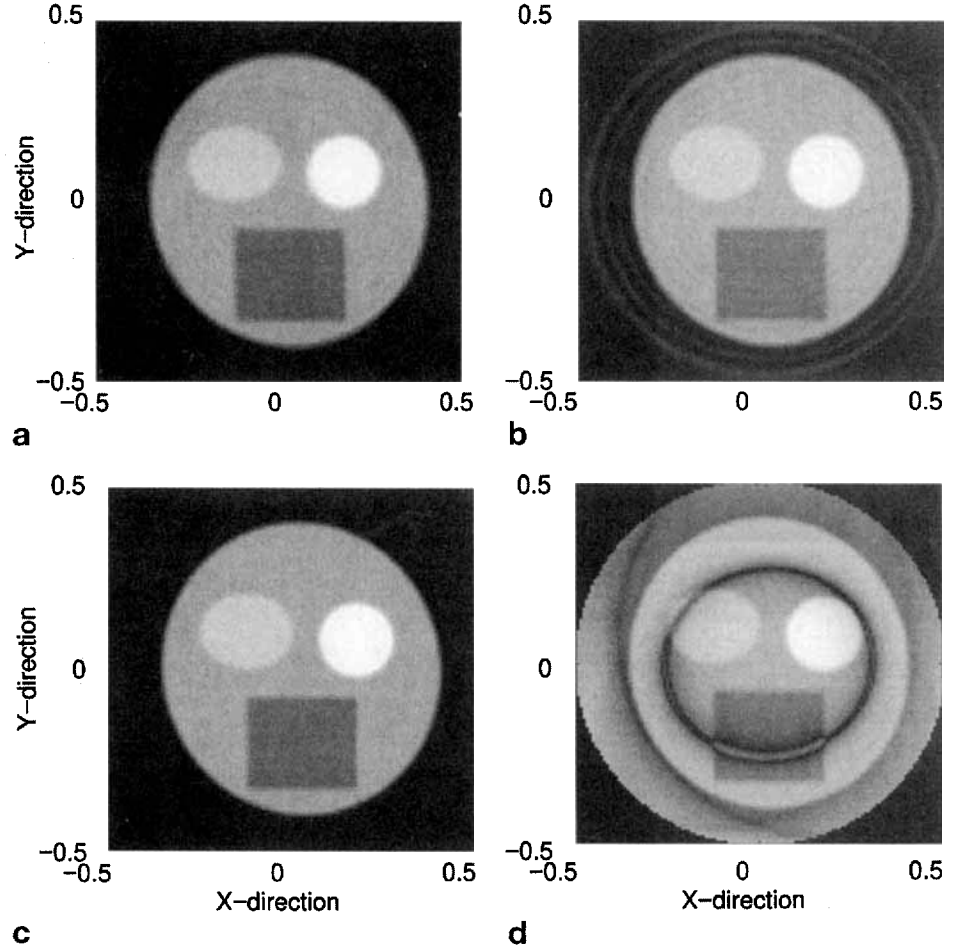


FIG. 4. Synthetic, noise-free, phantom images. (a) Reference $[128 \times 128]$ cartesian image reconstructed with the FFT. (b) Radially nonequidistant $[84 \times 200]$ polar k -data reconstructed with the 2D GRD algorithm. The radial spacing is about Δk_r at low frequencies but increases to over $3\Delta k_r$ at high frequencies. (c) The same k -data as in Fig. 4b, but reconstructed with the hybrid GRD/CBP algorithm. (d) Radially equidistant $[84 \times 200]$ polar k -data of radial spacing $1.52\Delta k_r$ reconstructed with the 2D GRD algorithm. The details of the k -data sample locations can be found in the text. All images were reconstructed onto a $[128 \times 128]$ image grid. Note the severe aliasing in Fig. 4d as compared with Fig. 4b or Fig. 4c, even though the matrix size and k -space extent are the same.

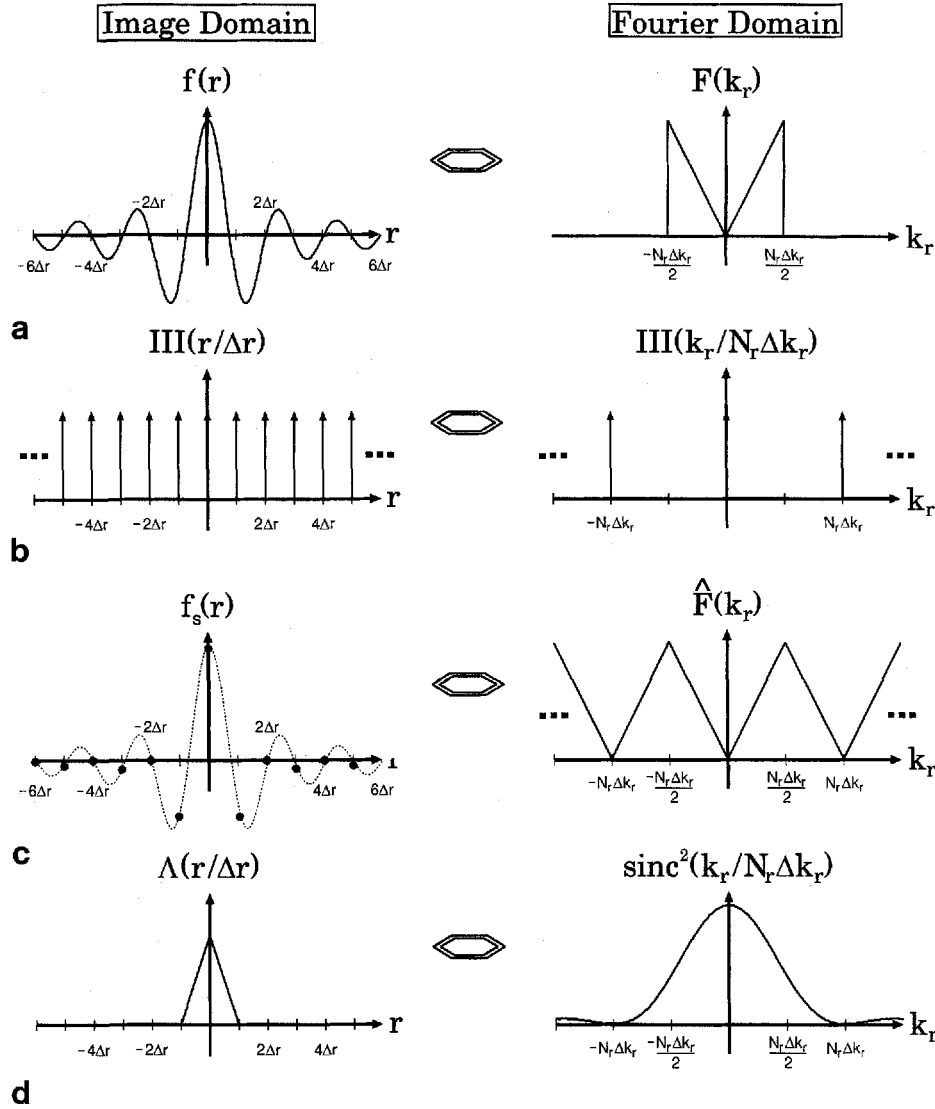


FIG. 5. Convolution backprojection MTF details in both the image domain (left side) and the Fourier domain (right side). (a) The ramp filter $F(k_r)$ and its corresponding IFT $f(r)$ in the image domain. (b) The 1D image domain sampling function of spacing Δr and its FT, a series of impulses with spacing $(1/\Delta r) = N_r\Delta k_r$. (c) The result of sampling gives $f_s(r)$, whose FT is $\hat{F}(k_r)$, a replicated version of the ramp filter. (d) The triangle function of width $2\Delta r$, and its FT, which is proportional to $\text{sinc}^2((k_r/N_r\Delta k_r))$. (e) Linear interpolation of $f_s(r)$ (i.e., convolution with the triangle function) and its FT given by $\hat{F}(k_r)$ apodized by the sinc^2 function. (f) An expanded view of $\hat{F}(k_r)\text{sinc}^2((k_r/N_r\Delta k_r))$ out to $\pm N_r\Delta k_r$. (g) The back-projection of $f_s(r) \star \Lambda(r/\Delta r)$ at angle k_θ onto the image grid, and its Fourier counterpart $\hat{F}(k_r)\text{sinc}^2((k_r/N_r\Delta k_r))$, which is centered at $(0, 0)$, oriented at angle k_θ , and wrapped around, due to 2D image domain sampling. (h) At $k_\theta = [0^\circ, 45^\circ]$, $\hat{F}(k_r)\text{sinc}^2((k_r/N_r\Delta k_r))$ wraps onto itself giving 1D profiles at $k_\theta = 0^\circ, 45^\circ$, respectively, in 2D Fourier space. (i) The wrap-around effect in the Fourier domain for k_θ not a multiple of 45° , shown here for $k_\theta = 22.5^\circ$.

where \mathcal{Q} and \mathcal{F}^{-1} are the spin integration and IFT operators, respectively, and \star is the convolution operator. In analogy to Eq. [11], spin integrating the IFT of the discrete weighting will produce ringlobes in the PSF.

In comparison, for the GRD/CBP reconstruction, the GRD portion requires a weighting of $|(dK(m\Delta k_r)/dk_r)|$. The ramp-like weighting is applied as a convolution in image space in the CBP portion of the algorithm via $C_{\text{cbp}}(r)$. The PSF is thus given by

$$\text{PSF}_{\text{grd/cbp}} = \mathcal{Q} \left\{ \mathcal{F}^{-1} \left[\left| \frac{dK(m\Delta k_r)}{dk_r} \right| \right] \star C_{\text{cbp}}(r) \right\} \quad [23]$$

where $C_{\text{cbp}}(r)$ is given in Eq. [14]. Note that before convolution, only the baseband is retained. Within this baseband, the aliasing effects of having undersampled at large k_r persist, which is reflected in the $\mathcal{F}^{-1}\{|(dK(m\Delta k_r)/dk_r)|\}$ term.

Now, comparison of Eqs. [22] and [23] shows that the only difference in the PSFs is the function convolved

with $\mathcal{F}^{-1}\{|(dK(m\Delta k_r)/dk_r)|\}$ before spin integration. In GRD/CBP, it is $C_{\text{cbp}}(r)$, which is calculated from the spin integration of the IFT of the *continuous* ramp-like function, namely Eq. [18]. Conversely, in 2D GRD, it is the IFT of the (nonuniformly) *sampled* ramp function. Thus, in analogy to the purely polar case, the ringlobes emanating from the IFT of the discrete k -space ramp weighting have been eliminated, although the original sampling effects (i.e., those due to undersampling of the high spatial frequencies) are retained within the baseband.

A simulation of radially nonequidistant polar k -data was conducted. The data were reconstructed using both 2D GRD and the GRD/CBP algorithms (Fig. 4). The reference image in Fig. 4a depicts the synthetic noise-free phantom k -data reconstructed from $[128 \times 128]$ cartesian samples of spacing Δk_r in both the k_x and k_y directions. Figures 4b and 4c show the 2D GRD and GRD/CBP reconstructions, respectively, of the same synthetic phantom sampled with radially nonequidistant polar sampling. The k -data consisted of 200 azimuthally equidistant sam-

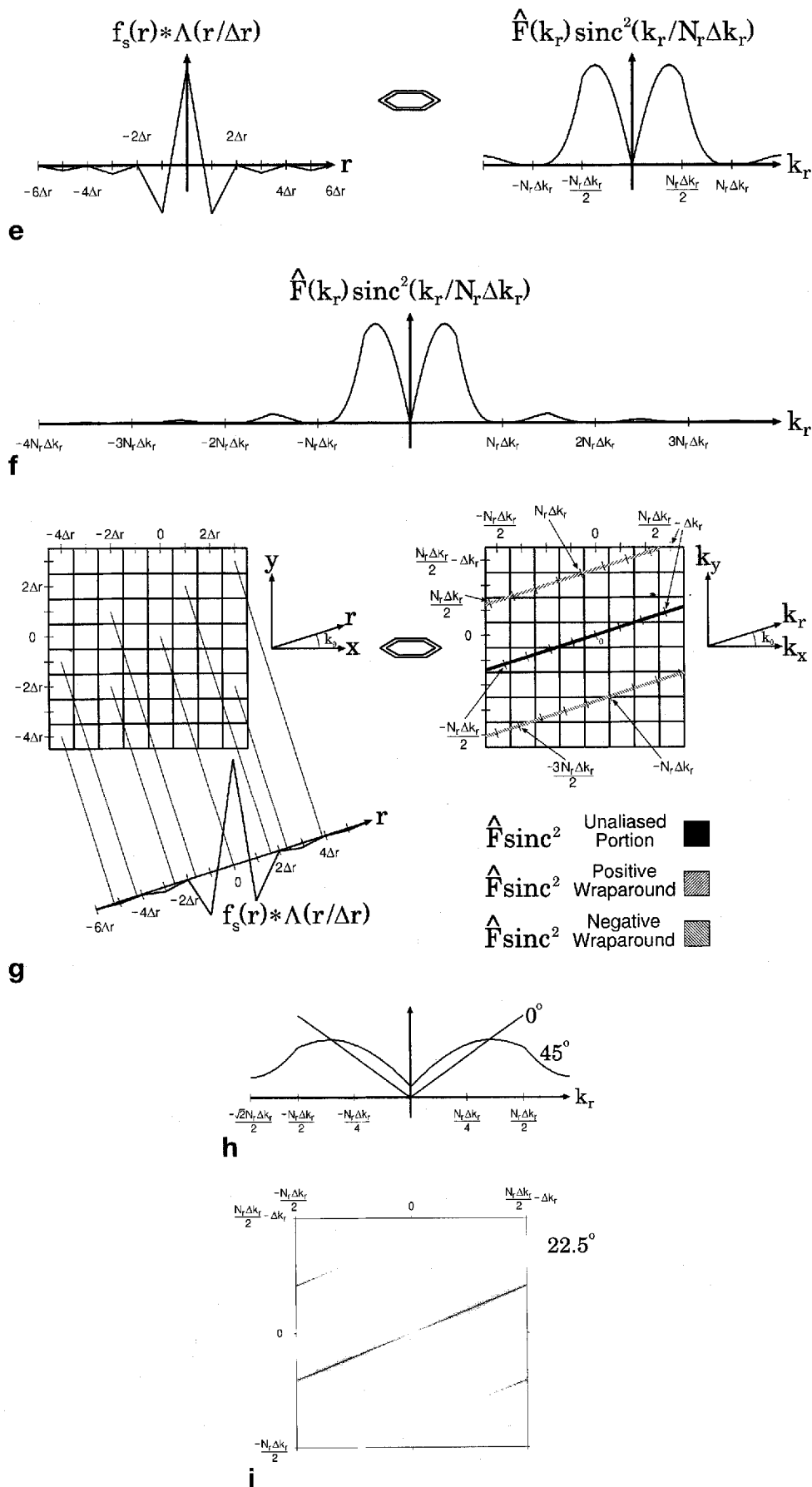


FIG. 5. Continued

ples within $(0, \pi)$ by M radial samples located at

$$K(k_r) = \pm \sum_{m=0}^{M/2} \left(\frac{k_r}{\Delta k_r} + c_5 \left[\frac{k_r}{N_r \Delta k_r} \right]^5 + c_{10} \left[\frac{k_r}{N_r \Delta k_r} \right]^{10} \right) \cdot \delta(k_r - m \Delta k_r) \quad [24]$$

where c_5 and c_{10} are constants, and $M < N_r$. By setting $c_5 = 5000$, and $c_{10} = 80,000$, we get $M = 84$, so that the radial extent is $128\Delta k_r$. This represents a 34% reduction of k_r samples. For comparison, Fig. 4d depicts the case of 84 radially equidistant polar samples covering the same k_r extent of $128\Delta k_r$ but with spacing $1.52\Delta k_r$.

Note that because the radial extent of \mathbf{k} -space is constant (see Fig. 3), all reconstructed images have the same pixel size. The aliasing effects, however, are different, especially when comparing the equidistant versus nonequidistant cases. Furthermore, the SNR and *effective* resolution differ, although these two effects must be considered jointly (as discussed in the Tradeoffs section).

In Fig. 4c, the circular oscillations present inside and outside the object are strictly due to undersampling at large k_r . They emanate mostly from the object boundary (outer ellipse), since the aliasing effect is more pronounced for large objects within the FOV. In Fig. 4b, the oscillations are slightly larger, especially in the region outside the object. This is the ringlobe effect arising from the $\mathcal{F}^{-1}[|K(m\Delta k_r)|]$ term in Eq. [22]. Moreover, the signal amplitude effect seen in Fig. 1 persists in Fig. 4b but is eliminated in Fig. 4c, since this, too, is a ringlobe effect. It emanates from the \mathbf{k} -space discretization of the ramp-like filter *before* IFT and subsequent spin integration.

Figure 4d clearly demonstrates that if the \mathbf{k} -space coverage and the number of samples is the same as in the radially nonequidistant case, the aliasing is severe, although the underlying gross characteristics of the object are still recognizable.

Neither the GRD nor GRD/CBP reconstructions correct for aliasing present due to undersampling of the data. Thus, some aliasing is inevitable under those sampling circumstances. However, not all aliasing is catastrophic. In fact, it may be possible to sample in such a way that the aliasing within the image is tolerable and does not affect the overall SNR and/or CNR (contrast-to-noise ratio) characteristics of the image too severely.

DISCUSSION

The image reconstruction effects of equidistant radial/azimuthal polar \mathbf{k} -data were investigated for both the gridding and the convolution backprojection algorithms. These effects included the SNR, resolution and the aliasing present in the image.

Although GRD is primarily a Fourier-domain algorithm and CBP is an image-domain technique, both of these algorithms perform identically in terms of SNR and resolution, provided that these two effects are considered together. In their most basic implementations, i.e., the

weighting based on ramp filters, GRD maximizes resolution at the expense of SNR, whereas CBP sacrifices resolution to increase the SNR.

The variance analysis presented herein yields the SNR value, an effectively global figure of merit. However, a more in-depth analysis of the noise power spectrum is warranted to ascertain and determine the complete characteristics of noise propagation within each algorithm.

Gridding offers the advantage of direct manipulation of the \mathbf{k} -space data. This allows one to tailor the resolution versus the SNR. Moreover, GRD allows for the possibility of nonequidistant azimuthal polar sampling whereby one can maximize resolution and SNR simultaneously.

In this study, we contrasted GRD using the ramp filter with CBP using the Ram-Lak (ramp) filter, the most direct comparison between the two algorithms. However, many choices of reconstruction weighting and/or convolution functions are possible for both GRD and CBP. In fact, the polar \mathbf{k} -data can be reconstructed using CBP and GRD such that the images have comparable SNR and resolution. In this case, either the GRD weighting function or the CBP convolution function, or both, must be altered to yield comparable variances and MTFs. Apodized ramp filters also have the added benefit of suppressing Gibb's ringing artifacts, but doing so leads to increased blurring and a loss of image resolution.

One important difference between GRD and CBP is their different PSFs, which lead to different aliasing behavior. The polar PSF using GRD includes the main lobe and the ringlobes. The main lobe describes the blurring effect of finite sampling, and the ringlobes are a measure of the expected aliasing. Conversely, the PSF using CBP eliminates the ringlobes altogether. Thus, provided the radial sampling satisfies the Nyquist criterion, the aliasing using CBP will be minimal. In both algorithms, however, insufficient azimuthal sampling leads to streaking artifacts in the image (azimuthal aliasing). Neither GRD nor CBP correct for this artifact.

Interestingly enough, simulations show that if the \mathbf{k} -data are radially continuous as opposed to discrete (i.e., spiral versus concentric circles), the PSF ringlobes are reduced, which leads to reduced aliasing. However, the spiral PSF is dependent on the number of interleaves acquired and, consequently, so is the aliasing. In short, one must fully characterize the PSF of the particular sampling scheme to ascertain the aliasing effects. Therefore, the conclusions drawn here for purely polar sampling do not necessarily apply to spiral sampling.

To reconstruct radially nonequidistant but azimuthally equidistant k -data, we suggested a hybrid GRD/CBP reconstruction algorithm. This technique reduces aliasing in comparison with 2D GRD, although the reconstruction times tend to be longer by about 30% or so. Although an in-depth analysis of the radial sampling effects of radially nonequidistant polar \mathbf{k} -data is beyond the scope of this study, the hybrid GRD/CBP algorithm may allow one to investigate the tolerable aliasing limits and ensuing tradeoffs of radially nonequidistant polar \mathbf{k} -space sampling.

APPENDIX A: CONVOLUTION BACKPROJECTION INTEGRAL

In polar coordinates, $k_x = k_r \cos k_\theta$ and $k_y = k_r \sin k_\theta$, from which the 2D IFT of $M(k_r, k_\theta)$ is

$$\begin{aligned} I(x, y) &= \int_{k_\theta=0}^{2\pi} \int_{k_r=0}^{\infty} M(k_r, k_\theta) e^{2\pi i k_r [x \cos k_\theta + y \sin k_\theta]} k_r dk_r dk_\theta \\ &= \int_0^\pi \int_0^\infty M(k_r, k_\theta) e^{2\pi i k_r X} k_r dk_r dk_\theta \quad [A1] \\ &\quad + \int_\pi^{2\pi} \int_0^\infty M(k_r, k_\theta) e^{2\pi i k_r X} k_r dk_r dk_\theta \end{aligned}$$

where $X = [x \cos k_\theta + y \sin k_\theta]$. In the second integral, we can first substitute $k_\beta = k_\theta - \pi$, then note that $M(k_r, k_\beta + \pi) = M(-k_r, k_\beta)$, and then substitute $k_s = -k_r$ to obtain

$$\begin{aligned} \int_{k_\theta=\pi}^{2\pi} \int_{k_r=0}^{\infty} M(k_r, k_\theta) e^{2\pi i k_r X} k_r dk_r dk_\theta \\ = \int_0^\pi \int_{-\infty}^0 M(k_s, k_\beta) e^{2\pi i k_s X} |k_s| dk_s dk_\beta \quad [A2] \end{aligned}$$

$$I(x, y) = \int_0^\pi \int_{-\infty}^{\infty} M(k_r, k_\theta) e^{2\pi i k_r X} |k_r| dk_r dk_\theta \quad [A3]$$

Now, for a particular $k_\theta = k'_\theta$, the $X(x, y)$ variable represents the projection of (x, y) -space at the same angle k'_θ in the image domain. Conversely, we can write this 2D $X(x, y)$ representation as a 1D representation of r in conjunction with backprojection:

$$\begin{aligned} \int_{-\infty}^{\infty} M(k_r, k'_\theta) e^{2\pi i k_r X(x, y)} |k_r| dk_r \\ \rightarrow \mathcal{B} \left\{ \int_{-\infty}^{\infty} M(k_r, k'_\theta) e^{2\pi i k_r r} |k_r| dk_r \right\} \quad [A4] \end{aligned}$$

$$= \mathcal{B} \{ \mathcal{F}^{-1}[M_{k'_\theta}(k_r)] |k_r| \} = \mathcal{B} \{ \mathcal{F}^{-1}[M_{k'_\theta}(k_r)] \star \mathcal{F}^{-1}[|k_r|] \}$$

where \mathcal{B} denotes backprojection, and $M_{k'_\theta}(k_r) \equiv M(k_r, k'_\theta)$ represents the radial k -line at angle k'_θ . Note that Eq. [A4] applies to continuous functions, whereby the ramp weighting can be applied as a multiplication in k -space or as a convolution in image space (by virtue of the Fourier convolution theorem [ref. 9, p. 108]). When applied to discrete functions, however, the convolution expression is preferred, since it does not suffer from cyclical aliasing (ref. 21, Ch. 7). Finally, then

$$I(x, y) = \int_0^\pi \mathcal{B} \{ \mathcal{F}^{-1}[M_{k'_\theta}(k_r)] \star \mathcal{F}^{-1}[|k_r|] \} dk_\theta \quad [A5]$$

The interpretation of Eq. [A5] follows readily. The IFT of each radial k_r -line at angle k_θ is convolved with the

IFT of the ramp filter, which compensates for the variable sample density. This convolved projection at angle k_θ is then backprojected for each desired image (x, y) location. The reconstructed image $I(x, y)$ is the summation of all the convolved projections at angles k_θ within $(0, \pi)$. Note that we imposed no conditions on $M(k_r, k_\theta)$ so that this reconstruction formalism is valid for Hermitian, anti-Hermitian, or non-Hermitian polar k -data.

APPENDIX B: CONVOLUTION BACKPROJECTION MTF/SNR DETAILS

One might expect the CBP MTF (using linear interpolation) to be given by $\mathcal{A}(k_r) \text{sinc}^2((k_r/N_r \Delta k_r))$ out to a maximum radius of $\frac{1}{2} N_r \Delta k_r$, where $\mathcal{A}(k_r)$ is the apodization function applied to the finite ramp filter. However, the discretization, interpolation, and resampling of the convolved data onto a cartesian grid leads to a more complicated MTF (see Fig. 2).

The MTF is given by the Fourier transform of the PSF, where we assume the object to be a point object so that each projection is given by a single impulse at $r = 0$, namely $\delta(r)$. The convolved projection is thus the IFT of the filter function. Here, we assume that the filter function is the Ram-Lak filter and that linear interpolation is used in the backprojection stage. The analysis depicted in Fig. 5 can be applied for other filters and more sophisticated interpolation schemes.

Figure 5a depicts the ramp filter $F(k_r)$ in the Fourier domain (on the right). Its IFT is

$$\begin{aligned} f(r) = \int_{-N_r \Delta k_r / 2}^{+N_r \Delta k_r / 2} |k_r| e^{2\pi i k_r r} dk_r = \frac{(N_r \Delta k_r)^2}{4} \\ \cdot \left[2 \text{sinc}(r N_r \Delta k_r) - \text{sinc}^2\left(\frac{r N_r \Delta k_r}{2}\right) \right] \quad [B1] \end{aligned}$$

which is depicted on the left of Fig. 5a (the image domain). For computation purposes, the convolution function is discretized at the Nyquist rate, namely $\Delta r = (1/N_r \Delta k_r)$. This discretization is expressed by multiplying $f(r)$ with the sampling function $\text{III}((r/\Delta r))$ of Fig. 5b to obtain $f_s(r)$, as shown in Fig. 5c. In Fourier space, this corresponds to convolving $F(k_r)$ with $\text{III}((k_r/N_r \Delta k_r))$ to give $\hat{F}(k_r)$, a replicated version of $F(k_r)$, as shown in Fig. 5c. The coefficients at locations $p \Delta r$ (where p is an integer) of $f_s(r)$ are

$$\text{Ram-Lak filter: } \left\{ \begin{array}{ll} 1/4 & p = 0 \\ -1/(p\pi)^2 & p \text{ is ODD} \\ 0 & p \text{ is EVEN} \end{array} \right\} \quad [B2]$$

The discrete $f_s(r)$ function is then (here assumed linearly) interpolated. Now, linear interpolation can be expressed as a convolution with a triangle function of width $2\Delta r$, e.g., $\Lambda((r/\Delta r))$, as depicted in Fig. 5d. This gives $f_s(r) \star \Lambda((r/\Delta r))$, which is shown in Fig. 5e. Note that this is effectively $C_{\text{cbp}}(r)$ of Eq. [14]. In Fourier space, this corresponds to $\hat{F}(k_r)$ being multiplied (apodized) by $\text{sinc}^2((k_r/N_r \Delta k_r))$, which is shown in Figs. 5e and 5f, the latter showing an expanded view.

With the interpolated $f_s(r)$ representing one projection at angle k_θ , we then backproject it onto the image grid at the appropriate (x, y) locations. This procedure is depicted in Fig. 5g. The 2D FT of this backprojected data results in $\hat{F}(k_r)\text{sinc}^2((k_r/N_r\Delta k_r))$ at the same angle k_θ in (k_x, k_y) -space. However, because of discretization in the x and y directions, we get wraparound (or folding) of the 1D function $\hat{F}(k_r)\text{sinc}^2((k_r/N_r\Delta k_r))$ in the 2D k -space (Fig. 5g).

If $k_\theta = 0$, then $\hat{F}(k_r)\text{sinc}^2((k_r/N_r\Delta k_r))$ is folded onto itself and is resampled with spacing Δk_r , which is the original sample spacing, and the foldover points occur at odd multiples of $\pm\frac{1}{2}N_r\Delta k_r$. In this case, we recover the ramp filter exactly, as shown in Fig. 5h. Similarly, if $k_\theta = 45^\circ$, then $\hat{F}(k_r)\text{sinc}^2((k_r/N_r\Delta k_r))$ also folds onto itself. However, unlike the $k_\theta = 0$ case, the foldover points occur at odd multiples of $\pm(1/\sqrt{2})N_r\Delta k_r$. The effective weighting at 45° is not a ramp, but rather an apodized ramp-like function that is non-zero at $k_r = 0$ and extends out to $|k_r| = (1/\sqrt{2})N_r\Delta k_r$. This too, is depicted in Fig. 5h. For cases in which k_θ is not a multiple of 45° , $\hat{F}(k_r)\text{sinc}^2((k_r/N_r\Delta k_r))$ is distributed over much of the 2D k -space, as shown in Fig. 5i.

When backprojecting numerous projections within the azimuthal range $0 - \pi$, one gets the PSF, whose 2D FT is the MTF (see Fig. 2). The noncircular symmetry of MTF and the fact that it is not restricted to within a diameter of $N_r\Delta k_r$ is due to the above-mentioned wraparound effect.

ACKNOWLEDGMENTS

The authors thank Drs. Ian Cunningham and Kecheng Liu for helpful discussions, and Mr. Craig Jones for the phantom relaxation measurements.

REFERENCES

1. W. N. Brouw, Aperture synthesis, in "Methods in Computational Physics" (B. Alder, S. Fernbach, and M. Rotenberg, Eds.), Vol. 14, pp. 131–175, Academic Press, New York, 1975.
2. F. R. Schwab, Optimal gridding visibility data in radio interferometry, in "Indirect Imaging," (J. A. Roberts, Ed.), pp. 333–346, Cambridge University Press, New York, 1983.
3. J. D. O'Sullivan, A fast sinc function gridding algorithm for Fourier inversion in computer tomography. *IEEE Trans. Med. Imaging* **4**, 200–207 (1985).
4. J. I. Jackson, C. H. Meyer, D. G. Nishimura, A. Macovski, Selection of a convolution function for Fourier inversion using gridding. *IEEE Trans. Med. Imaging* **10**, 473–478 (1991).
5. R. N. Bracewell, A. C. Riddle, Inversion of fan-beam scans in radio astronomy. *Astrophys. J.* **150**, 427–434 (1967).
6. P. R. Smith, T. M. Peters, R. H. T. Bates, Image reconstruction from finite numbers of projections. *J. Phys. A*, **6**, 361–382 (1973).
7. S. W. Rowland, Computer implementation of image reconstruction formulas, in "Image Reconstruction from Projections: Implementation and Applications" (G. T. Herman, Ed.), Vol. 32 ("Topics in Applied Physics"), pp. 9–79, Springer Verlag, New York, 1979.
8. J. W. Cooley, J. W. Tukey, An algorithm for the machine computation of complex Fourier series. *Math. Comput.* **19**, 297–301 (1965).
9. R. N. Bracewell, "The Fourier Transform and Its Applications," McGraw Hill, New York, 1986.
10. C. E. Metz, K. Doi, Transfer function analysis of radiographic imaging systems. *Phys. Med. Biol.* **24**, 1079–1106 (1979).
11. J. G. Pipe, J. L. Duerk, Analytical resolution and noise characteristics of linearly reconstructed magnetic resonance data with arbitrary k -space sampling. *Magn. Reson. Med.* **34**, 170–178 (1995).
12. W. A. Edelstein, G. H. Glover, C. J. Hardy, R. W. Redington, The intrinsic signal-to-noise ratio in NMR imaging. *Magn. Reson. Med.* **3**, 604–618 (1986).
13. A. Macovski, Noise in MRI. *Magn. Reson. Med.* **36**, 494–497 (1996).
14. R. N. Bracewell, A. R. Thompson, The main beam and ringlobes of an east-west rotation-synthesis array. *Astrophys. J.* **182**, 77–94 (1973).
15. M. L. Lauzon, B. K. Rutt, Effects of polar sampling in k -space. *Magn. Reson. Med.* **36**, 940–949 (1996).
16. R. N. Bracewell, Strip integration in radio astronomy. *Aust. J. Phys.* **9**, 198–217 (1956).
17. A. K. Jain, "Fundamentals of Digital Image Processing," Prentice-Hall, Englewood Cliffs, NJ, 1989.
18. G. N. Ramachandran, A. V. Lakshminarayanan, Three-dimensional reconstruction from radiographs and electron micrographs: II. Application of convolutions instead of Fourier transforms. *Proc. Natl. Acad. Sci. USA* **68**, 2236–2240 (1971).
19. A. Macovski, C. Meyer, A novel fast-scanning system, in "Proc., SMRM, 5th Annual Meeting, Montreal, 1986," pp. 156–157.
20. C. H. Meyer, B. S. Hu, D. G. Nishimura, A. Macovski, Fast spiral coronary artery imaging. *Magn. Reson. Med.* **28**, 202–213 (1992).
21. E. O. Brigham, "The Fast Fourier Transform," Prentice-Hall, Englewood Cliffs, NJ, 1974.